RSC Advances

PAPER

View Article Online
View Journal | View Issue

Cite this: *RSC Adv.*, 2019, **9**, 18070

Fe^{3+}-codoped ultra-small $NaGdF_4$:Nd^{3+} nanophosphors: enhanced near-infrared luminescence, reduced particle size and bioimaging applications†

Yabing Li,‡[ab] Fujin Li,‡[b] Yanan Huang,[b] Haiyan Wu,[ab] Jian Wang,[ab] Jin Yang,[ab] Qingbo Xiao[bc] and Hongzhen Lin*[ab]

Received 30th January 2019
Accepted 7th April 2019

DOI: 10.1039/c9ra00798a

rsc.li/rsc-advances

Small-sized lanthanide-doped nanoparticles (NPs) exhibiting superior near-infrared (NIR) luminescence properties are highly desired for bioimaging applications. Herein, Fe^{3+} ions are codoped in $NaGdF_4$:Nd^{3+} nanocrystals *via* a simple coprecipitation method, which can simultaneously reduce the particle size and enhance the downconverting NIR luminescence of the NPs. The NIR luminescence intensity reaches the maximum for the obtained sub-5 nm NPs when the doping concentration of Fe^{3+} is tuned to 20 mol%, which is ~1.7 times higher than that of the pristine 8.7 nm NPs without Fe^{3+} doping. After being modified with targeting molecules, the ultra-small $NaGdF_4$:Nd^{3+},Fe^{3+} NPs were successfully applied as luminescent probes for targeted NIR imaging of tumors in biological tissues. Moreover, they also show great potential as a high contrast agent for T2-weighted MRI imaging.

1. Introduction

Lanthanide (Ln^{3+})-doped fluoride nanoparticles (NPs) simultaneously exhibiting small particle size and strong photoluminescence (PL) intensity are in high demand for their potential application in bioimaging.[1–8] In particular, the trivalent neodymium (Nd^{3+}) doped NPs show superior optical properties in luminescent bioimaging as both their excitation and emission can be located at the near-infrared (NIR) region, which provides high penetration depth and signal-to-noise ratio in biological specimens.[9–12] For minimizing the potential interference in cellular systems and favoring the easier excretion from the body, ultra-small NPs with particle sizes of less than 6 nm are also necessary.[13,14] Unfortunately, the PL intensity of Ln^{3+} ions in ultra-small NPs is always diminished by the notorious size-dependent surface quenching. For example, Nd^{3+}-doped NPs with an average size of about 5 nm have been synthesized previously.[9,10] Although the absolute quantum yield of such ultra-small NPs is much higher as compared to the upconversion (UC) NPs involving multiplexed excitation processes, their NIR luminescence intensity is only ~25% of that for 15 nm-sized counterparts. Coating a layer of homo- or heterogeneous inorganic shell to eliminate the surface quenching is an effective way in enhancing the emission efficiency Nd^{3+} in the NPs.[11,15,16] However, the core–shell structure requires complicated multi-step synthesis processes and the shell coating inevitably causes the growth of particle size. Another effective strategy for enhancing the luminescence efficiency of Ln^{3+} is altering the crystal-field (CF) surroundings around Ln^{3+} by codoping with metal ions, in view that the optical transitions of Ln^{3+} are sensitive to their local coordination. Very recently, various metal ions, such as Li^+, K^+, Co^{2+}, Bi^{3+}, Sc^{3+}, Fe^{3+} and Mo^{3+}, have been successfully adopted to tailor the host lattice and modify the PL intensities of Ln^{3+} in the NPs.[17–23] Unfortunately, these studies are mainly focused on the UCNPs such as $NaYF_4$:Yb^{3+},Er^{3+}. So far, there is no report on improving the downconverting NIR luminescence of Nd^{3+} in small NPs by codoping with metal ions.

In this paper, we report the synthesis of Fe^{3+} doped $NaGdF_4$:Nd^{3+} NPs *via* a facile coprecipitation method. For the first time, enhanced NIR emission and reduced particle size are achieved at the same time by doping of metal ions. By further modifying the NPs with folic acid, targeted imaging of tumours in nude mouse can also be realized.

2. Experimental section

2.1 Materials

$GdCl_3$ (99.99%), $NdCl_3$ (99.99%), YCl_3 (99.99%) were purchased from Jinan Henghua Sci. & Tec. Co., Ltd. $FeCl_3$ (99.9%), folic

[a]School of Nano Technology and Nano Bionics, University of Science and Technology of China, Hefei, Anhui 230026, China

[b]i-Lab, Suzhou Institute of Nano-tech and Nano-bionics (SINANO), Chinese Academy of Sciences, Suzhou, 215123, China. E-mail: hzlin2010@sinano.ac.cn

[c]State Key Laboratory of Structural Chemistry, Fujian Institute of Research on the Structure of Matter, Chinese Academy of Sciences, Fuzhou, Fujian 350002, China

† Electronic supplementary information (ESI) available. See DOI: 10.1039/c9ra00798a

‡ These authors contributed equally to this work.

acid (FA, 97%), oleic acid (technical grade, 90%), 1-octadecene (ODE, 90%) were purchased from Sigma-Aldrich. Ammonium fluoride (NH_4F) and dimethylsulfoxide (DMSO, 99.99%) were purchased from Aladdin. *N*-hydroxythiosuccinimide sodium salt (NHS, 98%), 1-(3-dimethylaminopropyl)-3-ethylcarbodiimide hydrochloride (EDC) were purchased from Bailingwei Technology Co., Ltd. PEG phospholipid (DSPE–PEG (2000)–NH_2) was purchased from Avanti Polar Lipids. NaOH, ethanol, methanol, cyclohexane, and chloroform were purchased from Sinopharm Chemical Reagent Co, Ltd (China). All reagents were used as received without further purification.

2.2 Synthesis of Fe^{3+} doped $NaGdF_4$:Nd^{3+} NPs

Monodispersed $NaGdF_4$ NPs doped with Nd^{3+} (3 mol%) and Fe^{3+} (10, 20, 30, 40 mol%) were synthesized using a modified coprecipitation method. Briefly, 0.97-*x* mmol of $GdCl_3$, 0.03 mmol of $NdCl_3$, *x* mmol of $FeCl_3$ were added to a mixture of oleic acid (20 mL) and 1-octadecene (15 mL). The mixture was heated to 160 °C under nitrogen protection and remained for 30 min to form the lanthanide oleate complexes. After cooled down to room temperature (RT), 4 mL of methanol solution containing 4 mmol NaOH and 6.4 mmol NH_4F was added slowly, and stirred for 30 min at 70 °C to evaporate the methanol. Then, the mixture was slowly heated to 300 °C under stirring for 60 min. After cooling down to RT, the resulting NPs were precipitated by the addition of ethanol, separated by centrifugation, washed several times with ethanol and finally redispersed in cyclohexane.

For comparison, 30 nm-sized $NaYF_4$:Nd^{3+} NPs were also synthesized with the similar method, except that $GdCl_3$ was replaced by YCl_3, the NH_4F was replaced as 4 mmol, NaOH was replaced as 2.5 mmol, and finally maintained at 310 °C for 90 min.

2.3 Modifying the NPs with PEG (PEG-NPs)

In a typical experiment, a dispersion containing 25 mg of NPs and 5 mL of chloroform was added into a 50 mL round-bottom flask equipped with a magnetic stir bar, and then another 5 mL of chloroform solution containing 10 mg of DSPE–PEG was added. After gently stirring for 30 min, the solvent was evaporated by rotary evaporation, and the residual was readily dispersed in water. After ultrasonication for 5 min, the resulting dispersion was filtered through a 0.22 μm membrane filter and then kept at 4 °C for further use.

2.4 Target modification with folic acid (PEG-NPs-FA)

First, 30 mg of FA, 60 mg of NHS and 36 mg of EDC were dissolved in 6 mL of deionized water at room temperature, the pH value is controlled in the range of 7–8. Then, 4 mL of PEG-NPs-NH_2 with a concentration of 5 mg mL^{-1} was added, and stirred in dark for 24 h at RT, dialyzed in deionized water for 48 hours. Finally, the mixture was freeze-dried to obtain the yellow PEG-NPs-FA powder and stored at −20 °C.

2.5 Characterization

The powder X-ray diffraction (XRD) patterns of the samples were recorded by a BRUKER D8 Discover X-ray diffractometer (λ = 0.154 nm). Both transmission electron microscopy (TEM) and high-resolution TEM (HRTEM) measurements were performed using a Tecnai G^2 F20 S-Twin field-emission TEM equipped with the energy-dispersive X-ray spectrum (EDS). The concentration of Gd^{3+} was measured on an inductively Coupled Plasma Optical Emission Spectrometer (PerkinElmer ICP-OES 2100DV). Fourier transforms infrared spectroscopy (FTIR) was measured on a Perkin-Elmer IR spectrometer using the KBr pellet technique. Dynamic light scattering (DLS) experiments were carried out on an ALV-5000 spectrometer goniometer equipped with an ALV/LSE-5004 light scattering electronic and multiple Tau digital correlator and a JDS Uniphase He–Ne laser (632.8 nm) with an output power of 22 mW. The MR images were measured using a Bruker 11.7 T micro-MRI system. The NIR PL spectra were measured using an Applied Nano Fluorescence spectrometer (USA) at RT with an excitation laser source of 785 nm.

2.6 *In vivo* near-infrared imaging

Animal handling was carried out at the Animal Laboratory of Soochow University (Suzhou, China). All animal experiments were conducted in accordance with the university's guidelines and were approved by the university's ethics committee.

The NIR imaging *in vivo* was performed with a 640 × 512 pixel 2D InGaAs/SWIR camera (Photonic Science, UK) equipped with an 880 nm long-pass filter and an 1100 nm long-pass filter (Daheng Optics and Fine Mechanics Co., Ltd, China). A near-infrared lens pair SWIR-35 (Navitar, US) was used to focus the image onto the detector. The excitation light was provided by an 808 nm diode laser (Starway Laser Inc., China). For *in vivo* NIR imaging, 100 μL of PEG-NPs-FA (2 mg mL^{-1}) were intravenously injected in tail vein of a nude mouse. The mouse was scanned after post-injection of three hours under illumination of the 808 nm light at a power of 6.8 W and the exposure time of 100 s.

2.7 Cytotoxicity measurements

The cytotoxicity of the NPs was assessed by cell viability based on the MTT assay. The assay was performed in triplicate in the same manner. Briefly, HeLa cells were seeded into 96-well plates at a density of 1 × 10^4 cells per wells in 150 μL of media. After overnight growth, the cells were incubated with various concentrations of PEG-NPs-FA (0, 20, 50, 100, 200, 300, 400, 500, 600 μg mL^{-1}) for 24 h (37 °C, 5% CO_2). Then 100 μL of MTT solution (1 mg mL^{-1}) was added to each well and the cells were further incubated for 3 h at 37 °C. After the MTT solution was removed, 150 μL of DMSO was added to each well and the plate was gently shaken for 10 min to dissolve the precipitated violet crystals. The optical density (OD) was measured at 490 nm using a microplate reader (Perkin Elmer, Victor X4). Cell viability was evaluated as a percentage compared to control cells. The measured OD values of the blank, control, and experimental groups were coded as OD_{bla}, OD_{con}, and OD_{exp}, respectively. Cellular survival rates were calculated by,

$$\text{survival rate } (\%) = \frac{OD_{exp} - OD_{bla}}{OD_{con} - OD_{bla}} \times 100\%$$

3. Result and discussion

3.1 Synthesis and characterization

The $NaGdF_4$:Nd^{3+},Fe^{3+} NPs were synthesized *via* a facile coprecipitation method. The XRD patterns of the samples confirm the formation of hexagonal-phase structure $NaGdF_4$ (JCPDs: 00-27-0699) with no impurity peaks (Fig. 1a). Obviously, doping of Fe^{3+} ions has no effect on the crystal phase of $NaGdF_4$:Nd^{3+},Fe^{3+} NPs. The ionic radii of Fe^{3+} and Gd^{3+} are 0.64 Å and 0.94 Å, respectively, which render the replacement of Gd^{3+} by Fe^{3+} in the fluoride NPs.[24,25] The magnified diffraction peak of (111) at around 30° was also shown in Fig. 1a. As the Fe^{3+} doping concentration increases from 0 to 20 mol%, the diffraction peak (111) slightly shifts to the smaller angle, indicating that Fe^{3+} with smaller ionic radius was successfully doped into the lattice site of $NaGdF_4$ and thus decreased unit cell volume and interplanar spacing. However, as increasing the Fe^{3+} concentration, Fe^{3+} occupies the interstitial sites in the NPs and induces abundant defects, which leads to decrease of unit cell volume and enlargement of diffraction peak of (111). Similar unit cell volume shrinking or expanding can also be seen in the Fe^{3+}, Li^+ or Mo^{3+} doped upconversion NPs.[19–21,25] As shown in Fig. S1,† the EDX shows the presence of Gd, Na, F, Nd and Fe in $NaGdF_4$:Nd^{3+},Fe^{3+} NPs, further indicating that Fe^{3+} can be doped into the nanoparticles. The TEM and HRTEM images of the NPs are also shown in Fig. 1. It can be seen from Fig. 1b–f that the as-prepared NPs with Fe^{3+}concentraion varying from 0 to 40 mol% are all monodispersed in the solution. Moreover, the grain size of $NaGdF_4$:Nd^{3+} NPs can be facilely regulated by the dopant of Fe^{3+} ions. When the doping concentration of Fe^{3+} increases from 0 to 40 mol%, the particle size of the NPs gradually decrease from 8.7 to 4.4 nm (see also Fig. S2†). Similar phenomenon can be seen in the $NaYF_4$ NPs doped with high concentration of Li^+.[23] As shown in the Fig. 1g, the HRTEM image clearly shows the high crystalline nature of the $NaGdF_4$:Nd^{3+},Fe^{3+} NPs. The lattice fringes with a *d*-spacing of 0.304 nm agree well with the lattice spacing for the (110) plane of hexagonal-phase $NaGdF_4$.

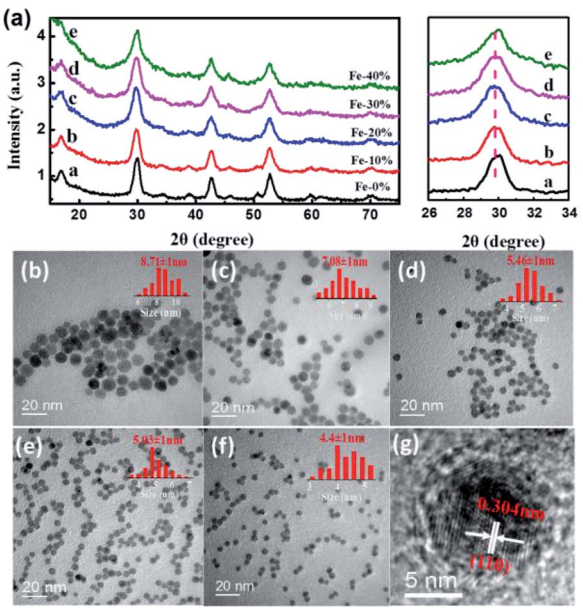

Fig. 1 Characterization of the $NaGdF_4$:Nd^{3+} NPs doping with different concentrations of Fe^{3+}. (a) XRD pattern of the NPs doping with different concentrations of Fe^{3+} and magnified view of main diffraction peak around 30°, (b) 0, (c) 10 mol%, (d) 20 mol%, (e) 30 mol% and (f) 40 mol%, respectively, and the inset is the particle size distribution of NPs, (g) HRTEM image of $NaGdF_4$:Nd^{3+},Fe^{3+} NPs.

3.2 Enhanced NIR emissions by Fe^{3+} doping

The NIR luminescence spectra of $NaGdF_4$:Nd^{3+},Fe^{3+} NPs were recorded upon excitation at 785 nm. As shown in Fig. 2, all the $NaGdF_4$:Nd^{3+},Fe^{3+} NPs exhibit two peaks centered at 1058 nm and 1335 nm in the NIR region, corresponding to the radiative relaxations from $^4F_{3/2}$ to the low-lying multiplets of $^4I_{11/2}$ and $^4I_{13/2}$, respectively. The shapes of NIR luminescence spectra for Nd^{3+} in $NaGdF_4$:Nd^{3+},Fe^{3+} NPs are similar to those in hexagonal-phase hosts such as $NaGdF_4$ NPs but quit different in terms of line positions, indicative of the incorporation of Nd^{3+} ions in the lattice site of $NaGdF_4$:Nd^{3+},Fe^{3+} NPs. Obviously, the doping of Fe^{3+} has a great influence on the NIR luminescence intensity of the $NaGdF_4$:Nd^{3+} NPs (Fig. 2a). The NIR luminescence intensity at 1058 nm and 1335 nm significantly enhances when the Fe^{3+} doping concentration increases from 0 to 20 mol%, and gradually attenuates as the further increment of Fe^{3+} concentration. The maximum NIR intensity of $NaGdF_4$:Nd^{3+} NPs doped with 20 mol% of Fe^{3+} is 1.7 times stronger than that of the Fe^{3+}-free counterparts (Fig. 2b). Previous researches have proved that the optical transitions of rare earth ions in inorganic hosts highly depends on their local coordination, and engineering the local structure of Ln^{3+} in the inorganic NPs has been regarded as a facile strategy for improving their luminescence intensity.[26–28] As has been discussed before, the doping of Fe^{3+} with small ionic radius in β-$NaGdF_4$ will regulate the local structure around Nd^{3+} in the crystal field. The volumetric shrinkage breaks the symmetry of the local crystal field around the Nd^{3+} ions, which leads to the high-sensitivity transmission and PL intensity enhancement of Nd^{3+} when the concentration of Fe^{3+}

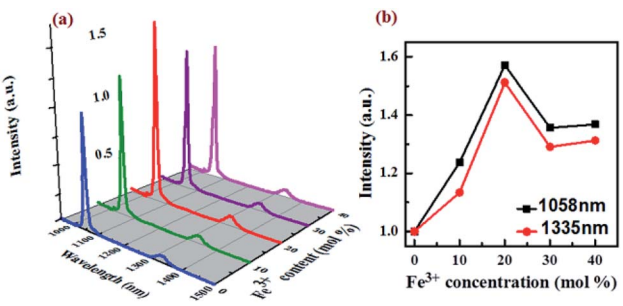

Fig. 2 (a) NIR luminescence spectra of $NaGdF_4$:Nd^{3+},Fe^{3+} NPs with Fe^{3+} doping concentration of 0–40 mol%. (b) Effect of Fe^{3+} doping on the NIR.

increase from 0 to 20 mol%. However, when the further increase the dopant content of Fe^{3+}, lots of lattice distortion and defects would appear due to excessive Fe^{3+} doping, which thus decrease the luminescence intensity of Nd^{3+}. The change of local crystal field around the Nd^{3+} by Fe^{3+} may also be reflected by difference in the radiative relaxations of $^4F_{3/2} \rightarrow {}^4I_{11/2}$ and $^4F_{3/2} \rightarrow {}^4I_{13/2}$. As can be seen in Fig. S3,† the integrated PL intensities of the band centered at 1058 nm are slightly stronger than those of at 1335 nm when doped with different concentration of Fe^{3+}, indicating that the doping of Fe^{3+} is a little more prone to increase the $^4F_{3/2} \rightarrow {}^4I_{11/2}$ transition as compared to $^4F_{3/2} \rightarrow {}^4I_{13/2}$.

3.3 Targeted NIR bioimaging

The as synthesized $NaGdF_4$:Nd^{3+},Fe^{3+} NPs are coated by hydrophobic oleic acid ligands and not suitable for the practical biological applications. The amphiphilic polymer DSPE–PEG (2000)–NH_2 was selected as capping ligands to convert the NPs into hydrophilic ones (PEG-NPs).[29–32] The NPs would become water-dispersible driven by the hydrophobic van der Waals interactions between the hydrophobic tail of the phospholipids and the primary oleate ligands on the NPs surface. The fatty acid chains of the phospholipids are embedded in the hydrophobic surface of the NPs, while the hydrophilic part points out toward the aqueous environment. In such a way, the surfaces of NPs can be modified with PEG, an inert, nontoxic, and non-immunogenic hydrophilic polymer.[33] Since DSPE–PEG–NH_2 has a reactive group –NH_2, (Fig. S9†). It can bind to the carboxyl group in FA. To facilitate targeted bioimaging in tissues, the NPs were further modified with the folic acid (FA) molecules (PEG-NPs-FA).[34–37] The schematic representation of the surface modification processes are shown in Fig. 3a. After surface modification, the size distribution of PEG-NPs and PEG-NPs-FA in aqueous solution was measured by DLS, and the hydrated particle sizes are determined to be 36 and 101 nm, respectively (Fig. 3b). The increase in hydrated size compared to the pristine nanoparticles may be due to the outward extension of the PEG phospholipid chain and slight aggregation of the NPs after surface modification. The stability of NPs in physiological medium was shown in Fig. S5–S7.† The successful modification of PEG and FA on the surface of nanoparticles was further demonstrated by FTIR. As shown in Fig. 3c, the pristine NPs, PEG-NPs and PEG-NPs-FA all exhibit broad absorption peaks centered at around 3438 cm^{-1}, which is corresponding to the stretching vibration of O–H bonds. After PEG modification, there is a significant enhancement of the peak at 2900 cm^{-1} ascribing to vibration of C–H band. Moreover, the tensile vibration of the C–O–C bond of PEG peak at 1110 cm^{-1} can also be observed, demonstrating the successful coating of PEG on the NPs. A new peak (1607 cm^{-1}) attributing to the stretching vibration of the –C=N bond of FA molecule can be observed in PEG-NPs-FA, which demonstrates the successful modification of FA at the NP surface. After FA modification, the zeta potential of the NPs change from 33.8 mV for PEG-NPs to −8.59 mV for PEG-NPs-FA due to the existence of –COOH in FA molecules (Fig. S4†). The amount of FA adsorbed was approximately 20% weight of the NPs. (Fig. S10†). After targeted modification of PEG and FA, the PEG-NPs-FA still retained strong NIR luminescence and relatively lower cytotoxicity (Fig. 3d and S8†), showing the excellent properties of the PEG-NPs-FA for bioimaging applications.

To test the ability of our sample for targeting imaging, nude mice with HeLa tumors were treated with PEG-NPs-FA. As can be seen in Fig. 4a, after 3 hours of injection into the tail vein, bright luminescence could be seen at the tumor under external 800 nm laser irradiation, demonstrating that PEG-NPs-FA can be used for targeted imaging *in vivo*. Since both the excitation and the emission are in the near-infrared range, the penetration depth can be greatly improved as compared to the visible lights.[38] In order to assess the dynamic flow, the images of mice were captured at different time periods. It can be seen that for

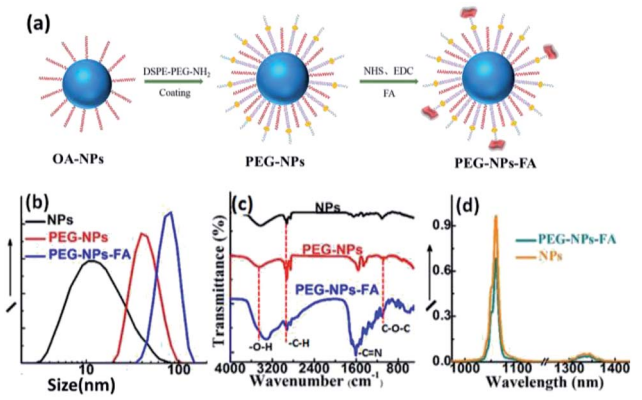

Fig. 3 Characterization of the targeted modification of $NaGdF_4$:Nd^{3+},Fe^{3+} NPs. (a) Schematic representation of the surface modification processes of the NPs, (b) DLS in aqueous solution, (c) FTIR and (d) NIR luminescence spectra of the NPs before and after ligand modification.

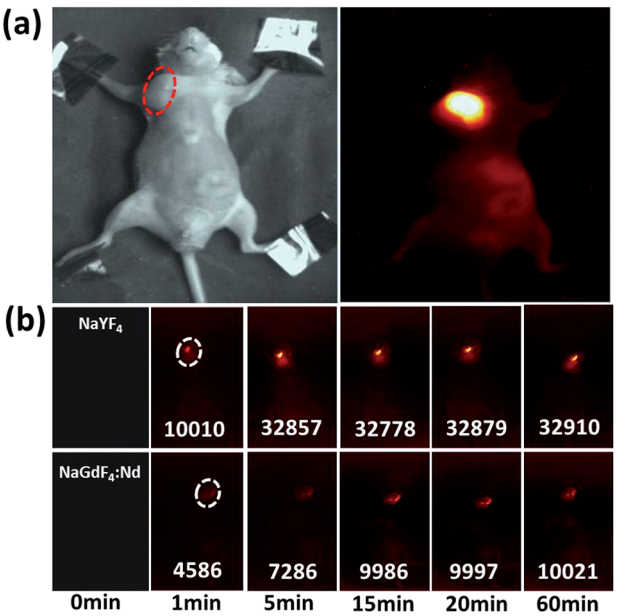

Fig. 4 (a) Targeted NIR imaging of the tumors by PEG-NPs-FA, and (b) comparison of the flow of the NPs with different hydrodynamic dimensions.

the PEG-NPs-FA with hydrodynamic dimension of ~101 nm, the NIR intensity at the tumor reaches the maximum within about 15 min, indicating that the NPs are accumulated at the tumor site in 15 min. For comparison, the NPs with hydrodynamic dimension of 150 nm were accumulated much faster at the tumor site, with the NIR intensity reaching the maximum in ~5 min (Fig. 4b and S11†). As shown in Fig. S12 in the ESI,† we also have used other mice for in targeting, For comparison, we have used PEG-NPs for non-targeted testing of other mice. The results show no passive accumulation of the nanoparticles in the tumor (Fig. S13†). Such phenomenon reflects that the smaller NPs are more prone to resist aggregation in tissues.

3.4 High contrast MR imaging

The longitudinal relaxation time (T_1) and transverse relaxation time (T_2) for different concentrations of PEG-NPs-FA were tested to evaluate their MRI properties. As can be seen in the Fig. 5a, b and S14a,† the MRI images of the NPs in aqueous solutions significantly enhanced with T2-weighted sequences as the increment of Gd^{3+} concentration. The obtained T_1 and T_2 values were plotted as $1/T_1$ (r_1) and $1/T_2$ (r_2) *versus* Gd^{3+} molar concentrations, respectively. The slope of these lines provides the molar longitudinal relaxivity r_1 and transversal relaxivity r_2, which are commonly used to evaluate the performance of MRI contrast agents.[38,39] Both experiments show a linear relation between concentration and relaxation times of protons. Obviously, the ratio of r_2/r_1 for $NaGdF_4$:Nd^{3+},Fe^{3+} NPs (25.63) (Fig. 5c) is much higher than that of $NaGdF_4$:Nd^{3+} (7.94) (Fig. S14b†). The large value of r_2/r_1 enables high contrast for T2-weighted MRI.[39–41] Obviously, doping of Fe^{3+} in the $NaGdF_4$:Nd^{3+} NPs can significantly increase the contrast of T2-weighted MRI under ultra-high magnetic field.

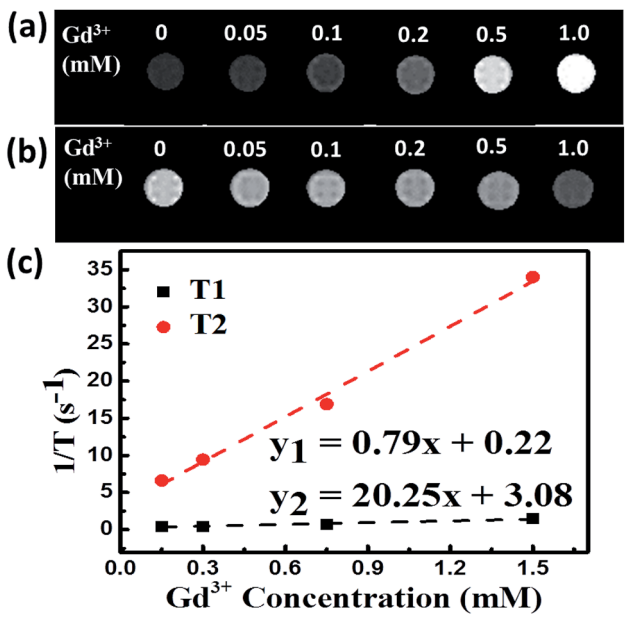

Fig. 5 (a) T1-, (b) T2-weighted MR images of $NaGdF_4$:Nd^{3+},Fe^{3+} NPs in aqueous solution as a function of Gd^{3+} concentration, (c) relationships between $1/T_1$ (black square) and $1/T_2$ (red circle) for the NPs of $NaGdF_4$:Nd^{3+}, Fe^{3+}.

4. Conclusion

We have synthesized the Fe^{3+}-doped $NaGdF_4$:Nd^{3+} NPs by a facile coprecipitation method. The doping of Fe^{3+} can significantly decrease the particle size and enhance the NIR luminescence intensity of the NPs simultaneously. Due to reduced local symmetry by Fe^{3+} doping, the NIR intensity increased by 1.7 times when the NPs size decrease from 8.7 nm to 4.4 nm. Through modification with targeting molecules, targeted NIR imaging of biological tissue tumors was achieved by the ultra-small $NaGdF_4$:Nd^{3+},Fe^{3+} NPs. The so-obtained NPs also show great potential in T2-weighted MRI imaging.

Conflicts of interest

There are no conflicts to declare.

Acknowledgements

This work is supported by the National Key Research and Development Program (2016YFA0200700), the National Natural Science Foundation of China (No. 21773294 and 21433013), the State Key Laboratory of Structural Chemistry, Chinese Academy of Sciences (20180029).

Notes and references

1 H. Fu, P. Peng, R. Li, C. Liu, Y. Liu, F. Jiang, M. Hong and X. Chen, *Nanoscale*, 2018, **10**, 9353–9359.
2 A. Gautam and P. Komal, *Coord. Chem. Rev.*, 2018, **376**, 393–404.
3 A. M. Kaczmarek, M. K. Kaczmarek and R. Van Deun, *Nanoscale*, 2019, **11**, 833–837.
4 B. Liu, C. Li, P. Yang, Z. Hou and J. Lin, *Adv. Mater.*, 2017, **29**, 1605434.
5 M. Liu, Z. Shi, X. Wang, Y. Zhang, X. Mo, R. Jiang, Z. Liu, L. Fan, C. G. Ma and F. Shi, *Nanoscale*, 2018, **10**, 20279–20288.
6 Q. Qiang, S. Du, X. Ma, W. Chen, G. Zhang and Y. Wang, *Dalton Trans.*, 2018, **47**, 8656–8662.
7 M. Wang, Y. Tian, F. Zhao, R. Li, W. You, Z. Fang, X. Chen, W. Huang and Q. Ju, *J. Mater. Chem. C*, 2017, **5**, 1537–1543.
8 W. You, D. Tu, W. Zheng, P. Huang and X. Chen, *J. Lumin.*, 2018, **201**, 255–264.
9 B. Liu, Y. Y. Chen, C. X. Li, F. He, Z. Y. Hou, S. S. Huang, H. M. Zhu, X. Y. Chen and J. Lin, *Adv. Funct. Mater.*, 2015, **25**, 4717–4729.
10 J. Peng, C. L. Teoh, X. Zeng, A. Samanta, L. Wang, W. Xu, D. Su, L. Yuan, X. Liu and Y.-T. Chang, *Adv. Funct. Mater.*, 2016, **26**, 191–199.
11 B. Zhou, W. Yang, S. Han, Q. Sun and X. Liu, *Adv. Mater.*, 2015, **27**, 6208–6212.
12 X. Li, X. Liu, D. M. Chevrier, X. Qin, X. Xie, S. Song, H. Zhang, P. Zhang and X. Liu, *Angew. Chem., Int. Ed. Engl.*, 2015, **54**, 13312–13317.

13 G. Tian, X. Zheng, X. Zhang, W. Yin, J. Yu, D. Wang, Z. Zhang, X. Yang, Z. Gu and Y. Zhao, *Biomaterials*, 2015, **40**, 107–116.
14 W. Zheng, D. T. Tu, P. Huang, S. Y. Zhou, Z. Chen and X. Y. Chen, *Chem. Commun.*, 2015, **51**, 4129–4143.
15 W. Zheng, P. Huang, D. T. Tu, E. Ma, H. M. Zhu and X. Y. Chen, *Chem. Soc. Rev.*, 2015, **44**, 1379–1415.
16 X. Li, R. Wang, F. Zhang, L. Zhou, D. Shen, C. Yao and D. Zhao, *Sci. Rep.*, 2013, **3**, 3536.
17 L. N. Sun, X. Q. Ge, J. L. Liu, Y. N. Qiu, Z. W. Wei, B. Tian and L. Y. Shi, *Nanoscale*, 2014, **6**, 13242–13252.
18 C. Dong, J. Pichaandi, T. Regier and F. C. J. M. van Veggel, *J. Phys. Chem. C*, 2011, **115**, 15950–15958.
19 G. Chen, T. Y. Ohulchanskyy, S. Liu, W.-C. Law, F. Wu, M. T. Swihart, H. Ågren and P. N. Prasad, *ACS Nano*, 2012, **6**, 2969–2977.
20 H. Yu, Q. M. Huang, E. Ma, X. Q. Zhang and J. C. Yu, *J. Alloys Compd.*, 2014, **613**, 253–259.
21 A. Xia, X. F. Zhang, J. Zhang, Y. Y. Deng, Q. Chen, S. S. Wu, X. H. Huang and J. Shen, *Biomaterials*, 2014, **35**, 9167–9176.
22 Y. Ding, X. Zhang, H. Gao, S. Xu, C. Wei and Y. Zhao, *J. Alloys Compd.*, 2014, **599**, 60–64.
23 Q. Cheng, J. Sui and W. Cai, *Nanoscale*, 2012, **4**, 779–784.
24 P. Ramasamy, P. Chandra, S. W. Rhee and J. Kim, *Nanoscale*, 2013, **5**, 8711–8717.
25 Y. Zhang, Y. Shen, M. Liu, Y. Han, X. Mo, R. Jiang, Z. Lei, Z. Liu, F. Shi and W. Qin, *CrystEngComm*, 2017, **19**, 1304–1310.
26 H. Wang and T. Nann, *ACS Nano*, 2009, **3**, 3804–3808.
27 J. Tang, L. Chen, J. Li, Z. Wang, J. Zhang, L. Zhang, Y. Luo and X. Wang, *Nanoscale*, 2015, **7**, 14752–14759.
28 D. Wang, B. Xue, X. Kong, L. Tu, X. Liu, Y. Zhang, Y. Chang, Y. Luo, H. Zhao and H. Zhang, *Nanoscale*, 2015, **7**, 190–197.
29 Q. Zhan, J. Qian, H. Liang, S. Gabriel, D. Wang, S. He, Z. Zhang and a. S. Andersson-Engels, *ACS Nano*, 2011, **5**, 3744–3757.
30 H. Lin, D. Xu, D. Teng, S. Yang and Y. Zhang, *Opt. Mater.*, 2015, **45**, 229–234.
31 T. Fan, Q. Zhang and Z. Jiang, *Opt. Commun.*, 2011, **284**, 1594–1597.
32 X. Chen, Z. Zhao, M. Jiang, D. Que, S. Shi and N. Zheng, *New J. Chem.*, 2013, **37**, 1782–1788.
33 L. L. Li, R. Zhang, L. Yin, K. Zheng, W. Qin, P. R. Selvin and Y. Lu, *Angew. Chem., Int. Ed. Engl.*, 2012, **51**, 6121–6125.
34 A. Basu, P. Upadhyay, A. Ghosh, D. Chattopadhyay and A. Adhikary, *ACS Biomater. Sci. Eng.*, 2018, **5**, 373–389.
35 Y. Li, J. Lin, X. Yang, Y. Li, S. Wu, Y. Huang, S. Ye, L. Xie, L. Dai and Z. Hou, *ACS Appl. Mater. Interfaces*, 2015, **7**, 17573–17581.
36 J. Wu, Q. Liu and R. J. Lee, *Int. J. Pharm.*, 2006, **316**, 148–153.
37 Z. Zhang and J. Yao, *AAPS PharmSciTech*, 2012, **13**, 802–810.
38 Y. Feng, Q. Xiao, Y. Zhang, F. Li, Y. Li, C. Li, Q. Wang, L. Shi and H. Lin, *J. Mater. Chem. B*, 2017, **5**, 504–510.
39 S. Biju, J. Gallo, M. Banobre-Lopez, B. B. Manshian, S. J. Soenen, U. Himmelreich, L. Vander Elst and T. N. Parac-Vogt, *Chemistry*, 2018, **24**, 7388–7397.
40 X. Jin, F. Fang, J. Liu, C. Jiang, X. Han, Z. Song, J. Chen, G. Sun, H. Lei and L. Lu, *Nanoscale*, 2015, **7**, 15680–15688.
41 H. Yang, Y. Zhuang, Y. Sun, A. Dai, X. Shi, D. Wu, F. Li, H. Hu and S. Yang, *Biomaterials*, 2011, **32**, 4584–4593.